Chapter 3
Interactions of Hydrogen with Lattice Defects

The potential energy of hydrogen atom close to lattice defects in metals is mostly lower than that in regular interstitial lattice sites due to elastic and electronic interactions as schematically shown in Fig. 1.1. Various lattice defects are produced in materials during thermal and mechanical processing, and the defects interact with hydrogen in their specific ways. The interactions are crucial for hydrogen embrittlement due to variations of hydrogen concentration around defects and to alterations of the densities and structures of defects. Observed hydrogen effects comprise contributions of various types of defects, but the separation of individual contribution is not easy.

3.1 Dislocations

3.1.1 Experimental Results

Hydrogen embrittlement takes place under applied stress more or less associated with plastic deformation. Dislocations are the primary player in plastic deformation, and hydrogen effects on mechanical properties have been ascribed mostly to interactions of hydrogen with dislocations. However, structures of dislocations associated with their movements are complicated like kinks, jogs, tangles and networks. Further, dislocation movements actually accompany creations of point defects like vacancies and interstitial atoms. Accordingly, the origin of hydrogen effects in plastic deformation is not simple, and experimentally determined parameters of interactions between hydrogen and dislocations must be carefully examined.

(a) Internal friction

Internal friction (IF) exhibits a specific response of dislocations to mechanical stimulations [1]. The IF is the dissipation of mechanical energy of vibration within

M. Nagumo, *Fundamentals of Hydrogen Embrittlement*,
DOI 10.1007/978-981-10-0161-1_3

the elastic range imposed on the specimen. It is normally expressed in terms of the reciprocal loss factor Q^{-1} defined as $\Delta W/2\pi W$, where W and ΔW are the maximum elastic stored energy and the energy dissipation during one cycle, respectively. The Q^{-1} spectrum against temperature rise for deformed iron exhibits two peaks, α- and γ-peaks, due to the movement of dislocations [1]. Various mechanisms of IF associated with the movement of dislocations have been proposed [2], and the α- and γ-peaks are ascribed to double-kink formation of non-screw and screw dislocations, respectively [3].

On the other hand, when hydrogen is introduced into deformed iron, a peak newly appears at intermediate between α- and γ-peaks, and it is named as the hydrogen cold-work peak (HCWP). An excellent correlation of the peak height with hydrogen concentration was observed [4]. The origin of HCWP is interactions of hydrogen with dislocations, but details are not straightforward. Hirth summarized three basic models of HCWP [5]. A simple model of dislocation motion is the string model of a damped oscillation between pinned points on a dislocation line. Schoeck's model is that dislocation drags hydrogen atmosphere as it bows out under oscillating stress [6]. Dislocation motion dragging hydrogen is a thermally activated process accompanying diffusion of neighboring hydrogen. The relaxation time τ of IF, the characteristic time to reach equilibrium, is temperature dependent since it is proportional to the concentration of hydrogen accumulated in dislocations and inversely proportional to the diffusion coefficient of hydrogen near the dislocation core. Then, τ is expressed in terms of the activation energy E_a which is the sum of the binding energy of hydrogen with dislocation E_b and the migration energy of hydrogen E_m. The magnitude of τ is obtained experimentally from the peak temperature vs. oscillation frequency relationship, i.e.,

$$2\pi f \cdot \tau = 1, \tag{3.1}$$

$$\tau = \tau_0 \exp\left(\frac{E_a}{RT}\right), \tag{3.2}$$

$$E_\mathrm{a} = E_\mathrm{b} + E_\mathrm{m}. \tag{3.3}$$

Estimation of E_b from observed E_a is somewhat ambiguous, since the mobility of hydrogen close to the core may differ from that in the bulk. For the case of high hydrogen concentrations close to saturation, E_a is simply equal to E_m.

Alternatively, kink-pair formation accompanying drag of hydrogen has been proposed for HCWP [7, 8]. The model is similar to that for α- and γ-peaks, and Eq. (3.3) is replaced by

$$E_\mathrm{a} = 2E_\mathrm{k} + E_\mathrm{m}^{'}, \tag{3.4}$$

where E_k is the kink formation energy and E'_m is the activation energy of diffusion along the core. In the literature, most estimations of E_b were made from experiments conducted following Schoeck's model, and reported values of E_b are around 25 kJ/mol in iron and steels [9–11] as tabulated in Table 3.1. The viability of an

Table 3.1 Experimentally estimated interaction energies of hydrogen with traps in cold-worked iron and steels

Material	Strain (%)	E_a (kJ/mol)	E_b (kJ/mol)	E_m (kJ/mol)	Measuring method	Note	Ref
Very high purity iron	10	32.6			IF		[9]
0.018 % C steel	15	29.6			IF		[9]
Pure iron	16	30	17–25	8.4–12.5	IF		[4]
High purity iron	25	35.1	27	8.4	IF		[10]
Mild steel	20	33	26	7	IF		[11]
Type 430 steel	20	75	43	32	IF		[11]
0.16%C steel	30		25		H-absorption		[12]
0.16%C steel	60		36		H-absorption		[12]
Ferritic steels			20		H-permeation		[12]
AISI 4340			30.5		H-permeation	High occupancy	[12]
0.23 % C steel			25		H-desorption	High occupancy	[12]
Pure iron	0–80		59.9		H-permeation	High occupancy	[13]

E_a, detrapping activation energy; E_b, binding energy; E_m,.migration energy; *IF* internal friction; high occupancy, under high hydrogen concentrations

employed model depends on experimental conditions such as microstructures, applied stress, temperature and hydrogen concentration.

(b) Hydrogen permeation

Trapping parameters are involved in the effective diffusion coefficient D_{eff}, Eqs. (2.16 and 2.17). which is obtained by permeation experiments. The temperature dependence of D_{eff} gives the apparent activation energy of permeation as included in the right-hand side of the equation:

$$\frac{\partial \ln D_{\mathrm{eff}}}{\partial (1/T)} = -\frac{E_m}{R} + \frac{K\mathrm{N}_x/\mathrm{N}_L}{1 + K\mathrm{N}_x/\mathrm{N}_L}\frac{E_b}{R}, \tag{3.5}$$

in the domain of low coverage [12]. Oriani analyzed data in the literature on hydrogen permeation or evolution for various steels with and without cold-work [12]. The estimated binding energies, E_b, were in the range of 25 ~ 35 kJ/mol, and the density of trapping sites, N_x, was of the order of 10^{25} m^{-3} in steels without cold-work. Both E_b and N_x increased with increasing amount of cold-work. However, Oriani suggested that microcrack surfaces are more important than dislocations for hydrogen trapping in cold-worked steels.

On the other hand, Kumnick and Johnson conducted hydrogen gas permeation-transient measurements for pure iron specimens given cold-work up to 60 % [13]. Kumnick and Johnson measured the time lag of the permeation and analyzed data using the McNabb-Foster equation for the diffusion accompanying trapping process. Details of permeation experiments and definitions of the time lag are described in Sect. 4.1. The time lag defined as the intersection of the integrated flux and the time axis varies according to the concentration of lattice hydrogen C_0 which is a function of the external hydrogen pressure following Sieverts' law given in Sect. 1.1. According to the McNabb-Foster equation, the time lag was expressed in terms of trap parameters p and k given in Eq. (2.22). The time lag with trapping, t_T, was proportional to the purely lattice time lag t_L, and the ratio t_T/t_L was shown to vary according to hydrogen pressure as schematically shown in Fig. 3.1 [13]. For the dilute occupancy region C in Fig. 3.1 for traps under low hydrogen pressures, t_T/t_L was independent of lattice hydrogen concentration and was approximated as

$$\frac{t_T}{t_L} = 1 + \mathrm{N}_T \frac{k}{p} = 1 + \frac{\mathrm{N}_T}{\mathrm{N}_L} \exp\left(\frac{E_b}{RT}\right), \tag{3.6}$$

where $\mathrm{N_T}$ and $\mathrm{N_L}$ are densities of trap and lattice hydrogen sites, respectively. On the other hand, for near saturation region A of traps under high hydrogen pressures, the ratio t_T/t_L was given as

$$\frac{t_T}{t_L} = 1 + \frac{3\mathrm{N}_T}{\mathrm{C}_0}. \tag{3.7}$$

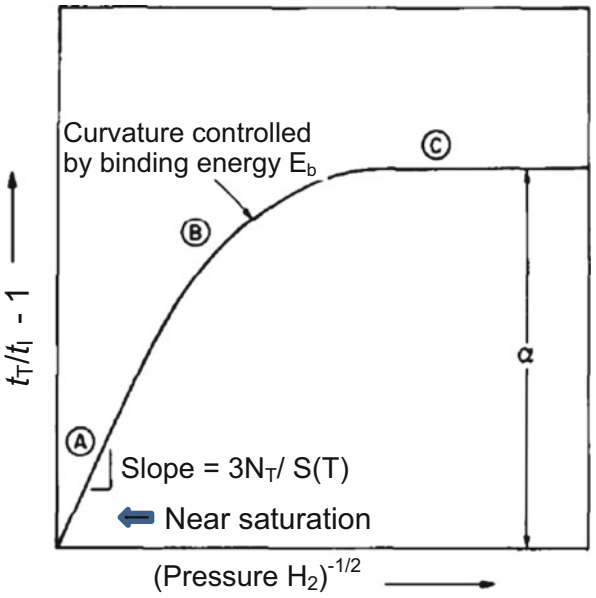

Fig. 3.1 Schematic diagram of variation of time lag with input hydrogen gas pressure for specimen with saturable traps. t_T and t_L are time lag with and without trapping. S(T) is Sieverts' law coefficient (Kummnick et al. [13])

Trap parameters were determined so as to fit calculated t_T/t_L with observed values. Thus, determined E_b was as high as 59.9 kJ/mol for iron given cold-work to 60 % at 318 K. Inferred trap densities were a little less than 10^{21} m^{-3} for annealed iron and a little more than 10^{23} m^{-3} for heavily deformed iron. Experiments were conducted under hydrogen gas pressures lower than 0.1 MPa. The pressure was fairly low, but observed time lags decreased with increasing hydrogen pressure, suggesting that experiments were in a range for saturated traps.

The entity of the trap corresponding to a high E_b of 59.9 kJ/mol is not definite. Kumnick and Johnson suggested some heterogeneous sites along dislocation core, like jogs or point defect debris left behind by moving dislocations. Kumnick and Johnson also noticed that sensitivities of experimental techniques to defects might differ by the range of trapping parameters.

Values of E_b and N_T obtained by IF and permeation experiments are included in Table 3.1. The materials were cold-worked iron and steels, and a single type of trap was assumed. The binding energies extending in a substantial range were not ascribed simply to dislocations. Multiple kinds of traps make transient permeation behaviors dependent on hydrogen concentration, and kinetics of filling traps differ by E_b of each trap as described in Sect. 2.2.2. Data obtained by IF techniques in Table 3.1 may be fairly reliable as interaction energies of hydrogen with dislocations in iron, but details of interactions as the origins of data obtained by different methods are not yet established experimentally.

(c) Thermal desorption analysis

The hydrogen absorption capacity in steels generally increases by plastic straining, indicating the increase in the density of lattice defects that trap hydrogen. Choo and Lee conducted TDA of hydrogen introduced to cold-drawn iron bar specimens of 5 mm in diameter [14]. Hydrogen was introduced under 0.2 MPa hydrogen pressure at 673 K, and TDA measurements were conducted after degassing mobile hydrogen at room temperature for 6 h. Application of Eq. (2.11) gave 19.2 kJ/mol for E_b after subtracting 7.6 kJ/mol for E_m from E_a. Choo and Lee assumed that remained hydrogen was trapped in dislocations and that desorption was dissociation-controlled. On the other hand, Ono and Meshii conducted TDA of hydrogen electrochemically introduced to a cold-rolled single crystal of pure iron. Assuming diffusion-controlled desorption under dynamic equilibrium between trapping and detrapping processes described in Sect. 2.1.2 (b), E_b of 47 kJ/mol gave good agreement between simulated and experimental TDA profiles [15].

The hydrogen absorption capacity increases associated with plastic straining, but the increase cannot be ascribed simply to dislocations. Figure 3.2 [16] shows the amounts of tritium introduced by cathodic electrolysis into low-carbon ferritic steel given tensile strain up to 25 % at 25 °C and −50 °C. The TDA measurement was conducted up to 800 °C, and the amount of tritium was expressed in terms of radioactivity. Thermal desorption almost totally took place in the temperature range between 120 and 150 °C showing a single desorption-rate peak. Tritium acts as the tracer of lattice defects, and the amount of desorbed tritium is a measure of the density of strain-induced defects. A noteworthy result was that the increase in the

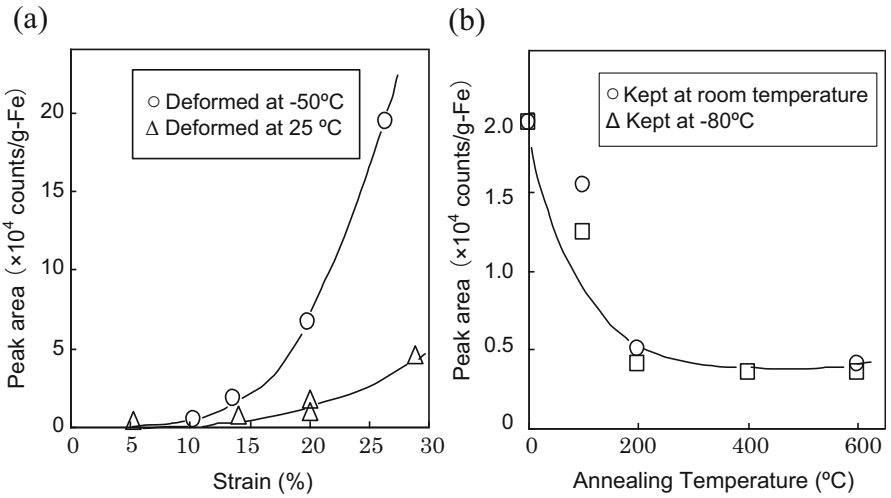

Fig. 3.2 Amounts of tritium absorbed in strained low-carbon ferritic steel. (**a**) Dependence on the amount of strain, (**b**) on the annealing temperature after straining by 20 % at −50 °C. Keeping temperature after straining was room temperature or −80 °C (Nagumo et al. [16])

hydrogen absorption capacity was almost totally reduced by aging the deformed specimens at temperatures as low as 200 °C. The density of dislocations must increase with strain, but annealing experiment implies that lattice defects concerned with the increase in absorbed tritium are point defects, mostly vacancies, rather than dislocations. The deformation temperature dependence of the hydrogen absorption capacity also implies that dislocations are not the primary sites of hydrogen trapping in this case. It is to be reminded that the partition of hydrogen among multiple traps is dependent on hydrogen fugacity as shown in Fig. 2.10. The cathodic electrolysis to introduce tritium in Fig. 3.2 was conducted using 1 N NaOH tritated aqueous solution at a current density of 25 A/m^3 for 2 h. The condition is fairly mild so as to avoid the formation of extraneous damage in the specimen. Further, Fig. 2.10 for the preferential partition of hydrogen at traps of different binding energies implies that deeper traps than dislocations, like vacancies, operate as predominant sites of hydrogen trapping.

3.1.2 Theoretical Estimation of Hydrogen-Dislocation Interactions

Interactions of dislocations with interstitial atoms such as carbon and nitrogen have been well accepted as the origin of yield point phenomena in steels. The interaction energy of a hydrogen atom with the elastic field of an edge dislocation is expressed as [17]

$$W = \frac{Gb\,(1+v)\,\delta \mathrm{v}\,\sin\,\theta}{3\pi\,(1-v)\,r}, \tag{3.8}$$

where G is shear modulus, b is Burger's vector, v is Poisson's ratio, δv is internal volume change around a hydrogen atom, r and θ are cylindrical coordinates fixed on the dislocation line. The volume change δv is 1.2 ml/mol in iron and is related to the partial molar volume V_{H} by

$$\delta \mathrm{v} = \frac{\mathrm{V}_H(1+v)}{3\,(1-v)}\,. \tag{3.9}$$

Then, the value of W is 28 kJ/mol for a hydrogen atom located at $r = 0.4$ nm and $\theta = \pi/2$. The elastic field of edge dislocation attracts hydrogen atoms, and Hirth and Carnahan numerically calculated the integral amount of hydrogen atoms in both the Boltzmann and Fermi-Dirac distributions [18]. Results in the two distributions beyond a critical inner cutoff radius of 0.248 nm were similar, but the use of the Fermi-Dirac distribution was necessary in a near core region.

An atomistic calculation of the distribution and the trap energy of hydrogen around an edge dislocation in iron was conducted by Taketomi et al. [19] The model dislocation was a $\{112\} < 111 >$ edge dislocation on a $\{112\}$ plane and the crystalline-disordered region was denoted as the dislocation core. Two types, tetragonal (T) and octahedral (O), of hydrogen occupation sites were considered and the energy of the system was calculated using an embedded atom method (EAM) potential. The hydrogen-trap energy is sensitive to both hydrostatic and shear stresses, and strong trap sites are distributed on the slip plane around the dislocation core. The calculated hydrogen-trap energy varies by the type of site and region around the dislocation core. The maximum trap energy in the core was about 42 kJ/mol. In outside of the core, the maximum trap energy was about 12 kJ/mol at a T-site below the slip plane, while O-sites showed much stronger trap energy in a region along the slip plane.

On the other hand, a straight screw dislocation has no long-range hydrostatic stress field. Elastic interaction with hydrogen appears in regions near wiggles on a flexible screw dislocation, leading to relatively weak and short-range elastic interactions. The origin of the high potential barrier has been attributed to core structures of screw dislocations [20]. Atomistic simulations with different methods have been conducted on the core structures and kink-pair formation [21–24].

Screw components of dislocations determine the mobility of dislocations in body-centered cubic metals at low temperatures, and thermal activation of kink pairs mediates the motion of screw dislocation. Wen et al. calculated the energy of a 1/2[111] screw dislocation introduced into a supercell in bcc iron using an EAM [25]. One hydrogen atom was placed at various sites in the core, and the binding energy of hydrogen was defined as the difference in energies between the states with and without hydrogen atom. The binding energies of hydrogen at thirteen sites available to hydrogen atom in the core were in the range between 43 and 4.3 kJ/mol.

On the other hand, Itakura et al. calculated the energy of screw dislocation using the density functional theory (DFT), placing a hydrogen atom at each T-site near the core [26]. The binding energy E_b of a specific site was defined as the hydrogen solution energy E_s referred to the bulk T-site. The expression of E_s was in the form

$$E_s = E_{d+H} - E_d - E_{H_2}/2, \tag{3.10}$$

where E_{d+H}, E_d and E_{H2} denote energies of a dislocation with a hydrogen atom, a reference dislocation configuration and a hydrogen molecule, respectively. Calculated values of E_b varied by the core configuration and site of hydrogen atom. The maximum values of E_b in the stable and unstable core configurations were 25 kJ/mol and 38 kJ/mol, respectively. The authors deduced that a hydrogen atom can lower the Peierls barrier by about 12.5 kJ/mol. Softening and hardening effects of hydrogen are expected by the reduction of either kink nucleation enthalpy or kink trapping, respectively. The calculations on the mobility of screw dislocations are further described in Sect. 5.5.2.

First-principles calculations of the electron structure affected by interstitial atoms in fcc iron were conducted by Gavriljuk et al. [27, 28]. The results were applied to the analysis of the interactions between dislocations and interstitial atoms. The calculations were for cases of fairly high hydrogen concentrations, 3 ~ 5 at% in atomic ratio [27] or 0.25 or 1.0 in an elementary cell [28]. The results are that hydrogen increases the density of conduction electrons in the vicinity of hydrogen atoms and lowers the shear modulus, the stress for the activation of dislocation sources, the line tension of dislocations and the distance between dislocations in the pileups. Similar effects as hydrogen are expected for nitrogen, but opposite for carbon because carbon decreases the density of conduction electrons around dislocations [27].

Interactions of hydrogen with dislocations strongly depend on structures of dislocations. Model structures of dislocations employed for theoretical estimations cited above are simplified for the convenience of calculation. Actually, densities of dislocations in steels that exhibit hydrogen embrittlement are very high and inhomogeneous segments on dislocation lines such as kinks, jogs, tangles and cell configurations induce complex stress and displacement fields.

Alternatively, Kirchheim developed an extensive theory on the stabilization of lattice defects by hydrogen in a thermodynamic scheme [29, 30]. By analogy with the Gibbs adsorption isotherm for a change in the surface energy by the adsorption of molecules, the total free energy of the system is reduced when solute atoms segregate at lattice defect. The reduction is ascribed to the decrease in the formation energy $d\gamma$ of the defect. The expression of $d\gamma$ in terms of the excess of solute at defect, Γ, and the change of the chemical potential on segregation, $d\mu$, for a solute A is in the form of

$$d\gamma = -\Gamma_A d\mu_A \,. \tag{3.11}$$

For dislocation, Γ_A was defined under constant temperature, volume and chemical potentials of A and the solvent as

$$\Gamma_A = \left.\frac{\partial n_A}{\partial l}\right|_{T,V,\mu_A,\mu}, \tag{3.12}$$

where l is the dislocation length and n_A is the number of A atoms under open system.

The decrease in the formation energy in the presence of hydrogen activates dislocation sources. Then, it was supposed that newly generated dislocations push former dislocations together with the ease of kink-pair formation and that the sequence appears as the observed enhanced mobility of dislocations by hydrogen [31]. This defect acting agent (DEFACTANT) mechanism is general and can be applied to formation energies of various defects such as dislocations, vacancies, grain boundaries and crack surfaces [31].

3.2 Vacancies

Vacancies play a crucial role in creep failure of metallic materials at high temperatures, but their role in hydrogen embrittlement has not been paid so much attention. Then, in order to understand interactions between hydrogen and vacancies, this section starts from some general attributes of vacancies.

3.2.1 Density

(a) Thermal equilibrium

The density of a single vacancy C_V in thermal equilibrium is given as [32, 33],

$$C_V = A\exp\left(-\frac{H_f}{RT}\right), \tag{3.13}$$

where A is the entropy factor of $1 \sim 10$ in most metals and H_f is the formation enthalpy of mono-vacancy. The magnitude of C_V is obtained directly from measured thermal dilatations subtracting the change of lattice constants, and the temperature dependence of C_V gives H_f. Reported values of C_V are very small, 2.4×10^{-11}, 1.3×10^{-21} and 7.6×10^{-27}, respectively, for Al, Cu and α-Fe at room temperatures with $A = 5$. It is to be noticed that observed C_V involves clustered vacancies [32]. The values of H_f are 65, 124 and 154 kJ/mol for Al, Cu and α-Fe, respectively.

Positron annihilation spectroscopy (PAS) is another powerful tool for measuring vacancy concentrations [32, 34]. Positrons injected into metal crystals migrate

through the lattice before annihilation with electrons, and the lifetime depends on the diffusional path. Vacancies effectively trap positron because of its relatively long lifetimes owing to low electron densities. The positron lifetime in vacancies is enhanced by 20 ~ 80 % to that in the perfect lattice. The positron-trapping probability in vacancies is proportional to the vacancy concentration. The trapping rate κ_v is expressed as

$$\kappa_v = \mu_v C_V , \tag{3.14}$$

where μ_v is the specific trapping rate for mono-vacancy and is estimated to be $(1.1 \pm 0.2) \times 10^{15}$/s [35]. The value of κ_v is determined from observed positron lifetime.

Positron annihilation is detected by measuring γ-ray emitted at the time of annihilation. Doppler broadening of annihilation γ-rays is utilized to distinguish annihilations with core and conduction electrons. The formation enthalpy H_f is calculated from observed Doppler broadening by using a trapping model. The obtained values of H_f for pure iron are 173 and 193 kJ/mol in the paramagnetic and ferromagnetic state, respectively [36]. Applications of PAS to hydrogen effects on lattice defects are presented in following Sects. 3.2.2 and 3.2.3(b).

(b) Generation associated with plastic deformation

The density of vacancies substantially increases associated with plastic deformation. The density of point defects amounting to 4×10^{-5} was estimated from electrical resistivity measurements on annealing iron strained to 20 % [37]. The observed density of point defects is ascribed mostly to vacancies because of the lower formation energy of vacancy than that of interstitial.

Generation of vacancies by mutual interactions of moving dislocations is well accepted. Van Bueren considered randomly distributed dislocations that form a spatial network [38]. Each element of the network can act as dislocation sources, and a generated dislocation loop crosses dislocations and forms jogs. The density of point defects left behind in the wake of moving jogs on the dislocation was estimated as $1.3 \times 10^{21} \varepsilon^2/\text{cm}^3$ in the case of multiple glide in copper. Cuttiño and Ortiz considered the motion of jogged screw segments formed by dislocation intersection and by double cross slip [39]. Computed vacancy concentrations in a uniaxial tension test on copper single crystal oriented for single slip are shown in Fig. 3.3 [39]. Quadratic dependence on strain appears in the multiple glide region, and the expected C_v is as high as 10^{-4} at strain of 30 %. An alternative mechanism of generating a high density of vacancies is mutual annihilation of dislocations of opposite signs approaching on closely neighboring glide planes [40]. The density of point defects depends on the density of dislocations, and a high concentration ~ 10^{-3} is expected for vacancies in the dislocation-rich walls of persistent slip bands in fatigued copper [40].

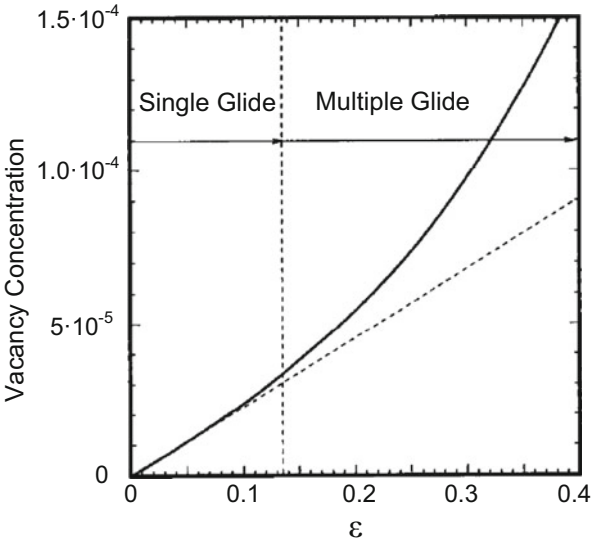

Fig. 3.3 Vacancy generation by the motion of jogged dislocations vs. axial strain (Cuttiño et al. [39])

3.2.2 Vacancy Clusters and Migration

Vacancy clusters and vacancy-impurity complexes are formed during migration, and the energies of vacancies are reduced by forming clusters. The formation enthalpy of a vacancy cluster of order n, $H_{f,,nv}$, is defined as

$$H_{f,\,nv} = nH_{f.\,1\,v} - H_{b,nv}\,, \tag{3.15}$$

where $H_{b,nv}$ is the binding enthalpy of a n-cluster. The $H_{b,nv}$ depends on the configuration of the vacancy cluster and a first-principles calculation of $H_{b,nv}$ was conducted for various configurations in α-iron [41]. The most stable configurations of n-vacancies in bcc structures are compact clusters, followed in order of decreasing stability by double layers, linear chains, tetravacancies, single layers, trivacancies and divacancies. Calculated dissociation energies of vacancy clusters of $V_n \rightarrow V_{n\text{-}1} + V_1$ increase with increasing cluster size, i.e., 85, 94, 117,140 kJ/mol for $n = 2$, 3, 4, 6, respectively, and almost constant for $n > 6$.

Positron annihilation spectroscopy is a useful tool for detecting vacancy clusters, and positron states thereof have been calculated using the density functional theory (DFT) [42]. Calculated positron binding energies and lifetimes for vacancy clusters shown in Fig. 3.4 [42] are listed in Table 3.2 [42]. When multiple traps are present, the observed positron lifetime τ is a weighted mean of lifetime components τ_i in each trap, i.e.,

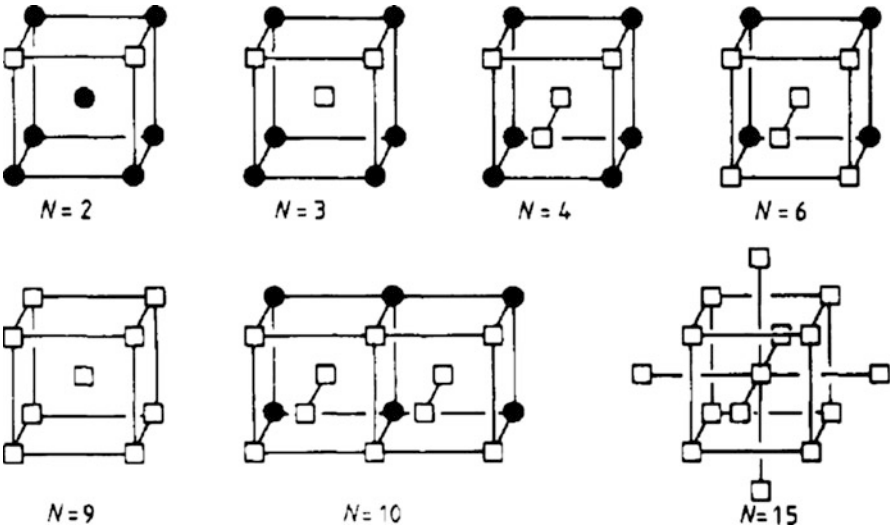

Fig. 3.4 Vacancy agglomerates in bcc structures. N is the number of vacancies (open square) in the agglomerate. *Filled circles* denote lattice sites (Puska et al. [42], Reprinted with permission from IOP Publishing)

Table 3.2 Calculated positron lifetime τ and binding energy E_b in vacancy clusters in Fe and Ni

Number of vacancies		1	2	3	4	6	10(Fe) 13(Ni)
Fe	τ(ps)	190	197	232	262	304	334
	E_b(eV)	3.0	4.0	5.6	6.6	7.7	8.6
Ni	τ(ps)	184	203		263	288	376
	E_b(eV)	2.6	3.8		5.9	6.8	9.2

Puska et al. [42], Reprinted with permission from IOP Publishing

$$\tau = \sum_{i=1}^{N} I_i \tau_i \,. \tag{3.16}$$

On isochronal annealing from 77 K for high-dose electron-irradiated pure ion, two-step decrease at about 220 and 350 K appeared as shown in Fig. 3.5 [35] for the short positron lifetime component τ_1 in a two-components analysis of τ. Alternatively, a long-lifetime component τ_2 appeared at 220 K, extended its value gradually on increasing the annealing temperature and finally disappeared at about 500 K. The decrease in τ_1 and the appearance of the τ_2 component at 220 K were ascribed to the thermally activated mobilization of mono-vacancies introduced by irradiation and the formation of small clusters. Successive increase in τ_2 was likely due to the increasing cluster size as shown in Table 3.2. The disappearance of τ_2 component at 500 K was ascribed to full annealing out of vacancy clusters and annihilation of dissociated vacancies [35].

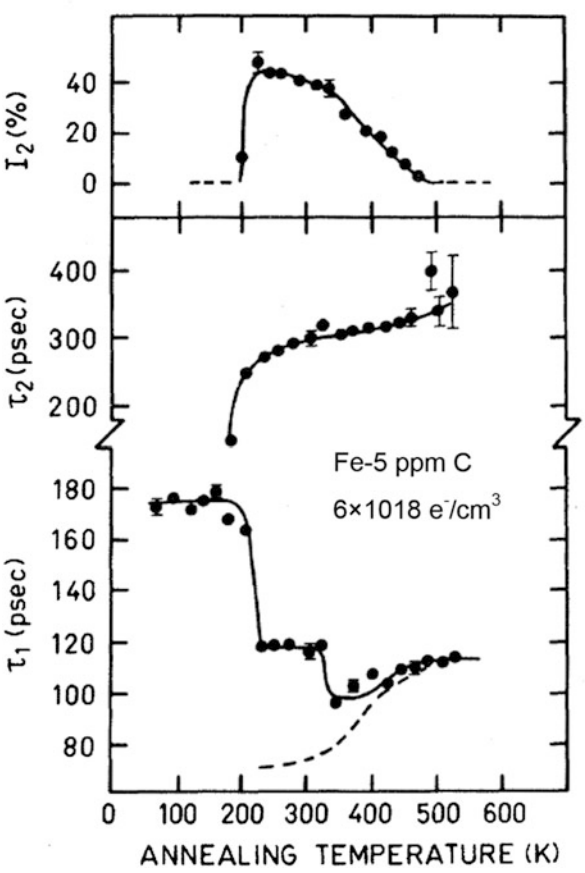

Fig. 3.5 Positron lifetime parameters vs. isochronal annealing temperature in the high-dose electron-irradiated pure iron (Vehanen et al. [35], Reprinted with permission from American Physical Society)

Interstitial impurities trap migrating vacancies and free carbon atoms form carbon-vacancy pairs or complexes [35]. For iron carbon-doped by 50 and 750 ppm, the decrease in τ_1 at 220 K indicated that the tendency of vacancies to form clusters decreased with carbon addition. For iron carbon-doped by 750 ppm, the short positron lifetime τ_1 after the drop at 220 K kept a higher level than that in pure iron [35]. The phenomenon was ascribed to the capture of migrating vacancies by carbon atoms, forming immobile carbon-vacancy pairs at the expense of forming vacancy clusters. The positron lifetime of the carbon-vacancy pair was estimated to be about 130 ps, much less than 190 ps for mono-vacancy. It was also suggested that the onset of free migration of carbon at 350 K caused further decoration of carbon-vacancy pairs that no longer had positron-trapping capability. The capability of positron capture of carbon-vacancy complexes is likely less than vacancy clusters, but it still remains on isochronal annealing above 350 K and disappears at 500 k due to the dissociation of the complexes [35].

Vacancies are mobile even at temperatures as low as 220 K in α-iron, but large three-dimensional clusters are immobile. The smallest immobile cluster is the tetravacancy. From the growth rate of interstitial-type dislocation loops introduced by electron irradiation, the estimated activation energy of migration of a single vacancy in iron was 120 kJ/mol [43]. On the other hand, calculated migration energies of mono-, di- and trivacancies in α-iron are in the range of 63.7–65.6 kJ/mol [41]. It is to be noticed that vacancy clusters must dissociate in order that the migration of vacancies takes place. In fcc metals such as Au, Al and Pt, calculated migration energies are in decreasing order from mono- to trivacancies [44]. A possible reason is that relatively loosely bound trivacancy is more mobile than divacancy which in turn is more mobile than mono-vacancy [44]. The disappearance of positron capture at 500 K implies that the dissociation of vacancy clusters takes place and that migrating vacancies annihilate in sites such as dislocations, grain boundaries and surfaces.

Electrical resistivity measurement is also used to detect lattice defects. Resistivity of pure iron increases by cold-work, and the strain-induced resistivity recovers on isochronal annealing. The recovery that took place from room temperature to 673 K was rather gradual, and then two stages appeared, the one centered around 753 K and the other distinctly at 823 K [37]. The continuous recovery up to 713 K was ascribed to the annihilation of point defects that amounted to the density of 10^{-5}. The further recovery was ascribed to the reduction in the density of dislocations that amounted to 10^{10} cm^{-2}. Annealing out of vacancy clusters at about 600 K and of dislocations at above 800 K was also detected by means of PAS for pure iron plastically deformed by 60 % [35].

It is to be noticed that the temperature at which recovery takes place on isochronal annealing varies not only by the presence of impurities but also by the concentration of vacancies. Decrease in the recovery temperature associated with increased quenching temperatures was observed in Au and Al corresponding to increased concentrations of quenched in vacancies [44].

3.2.3 Interaction of Hydrogen with Vacancies

(a) Binding energy and trapping configuration

Measurements of the binding energy of hydrogen with vacancies in metals were conducted extensively by Myers et al. by means of deuterium implantation methods [45–50]. Deuterium was ion-implanted at 15 keV into pure iron and formed a deuterium-rich zone close to the surface accompanying irradiation-induced defects [45]. Subsequent temperature ramp caused diffusion of deuterium. The concentration of deuterium in the implanted zone was detected using a 0.7 MeV ^{3}He ion beam that yielded counting protons by the D(^{3}He, p) ^{4}He nuclear reaction on the impingement. The release of deuterium from the implanted zone took place in two stages on the temperature ramp, and each stage was modeled mathematically using diffusion

Table 3.3 Binding energies of deuterium with vacancies produced by ion implantation

Material	$E_{V\text{-}H}$ (kJ/mol)	Type of vacancies	Ref.
Fe	46	Monovacancy	[45]
Fe	51	Monovacancy	[46]
Fe	68	Cluster	[46]
Fcc stainless steels	22	Cluster	[47]
Ni	23	Monovacancy	[48]
Ni	41	Multi-Vacancy	[48]
Cu	41	Monovacancy Small cluster	[49]
Mo	111	Cluster	[50]
Mo	99	Monovacancy (Low occupancy)	[50]
Mo	77	Monovacancy (High occupancy)	[50]

equations of the McNabb-Foster type, Eqs. (2.21 and 2.22), which included trapping terms. Trapping parameters were determined numerically so as to fit the theoretical calculation to experimental data. A sharp release stage centered around 260 K was ascribed to the migration of detrapped deuterium from deuterium-monovacancy pairs of 46 kJ/mok in the binding enthalpy. The successive stage in 350–450 K was ascribed to detrapping from a small vacancy cluster with the binding enthalpy of about 78 kJ/mol [45]. The figures were corrected later to 51 and 69 kJ/mol, respectively, in a modified experiment that suppressed the loss of deuterium from the surface [46].

Binding enthalpies of hydrogen with vacancies in various metals obtained by ion-implantation methods are listed in Table 3.3. In austenitic stainless steels, all release data of deuterium are approximately consistent with trapping at a single binding enthalpy of ~22 kJ/mol [47]. It is also to be noticed that the binding energy with vacancies alters by multiple trapping of hydrogen as described shortly.

Experimentally obtained binding enthalpies were theoretically rationalized referring to the location of hydrogen atom neighboring vacancies. Experimentally, a ^{3}He ion-channeling measurement for deuterium in an iron single crystal with the binding energy of 46 kJ/mol revealed that the deuterium atom displaced by 0.04 nm from the octahedral position along a $<100>$ direction toward a nearest-neighbor vacancy site [45]. The reason for the displacement is that a deuterium atom seeks the optimum electron density so as to minimize its energy. The binding energy of hydrogen atom calculated using an effective medium theory (EMT) was consistent with the observed one when a displacement of 0.05 nm was assumed [51].

There are 6 *O*-sites and 8 or 24 *T*-sites in fcc or bcc structure, respectively, around a vacant lattice site. Multiple occupations by hydrogen were deduced experimentally from ion-implantation experiments of deuterium with different fluencies. Figure 3.6 [52] shows effects of deuterium fluence on retained concentrations of deuterium in the implanted zone in iron after a linear temperature ramp. A decrease in the deuterium concentration appeared at 220 K, and the decrease was

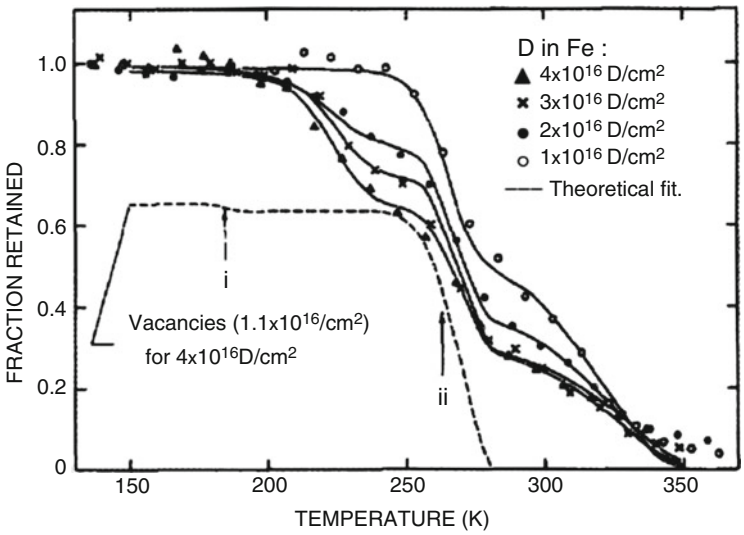

Fig. 3.6 D retention vs. temperature profile of 15-keV D in Fe. Strong He traps at 1.2 μm act as sinks for the released D (Besenbacher et al. [52], Reprinted with permission from AIP Publishing LLC)

enhanced with increasing deuterium fluence. The shift of the start of deuterium migration to lower temperatures associated with higher fluences was ascribed to the release of deuterium from multi-trapped states at mono-vacancy when the binding energy decreased with the increasing number of trapped deuterium atoms.

Binding enthalpies were also calculated using EMT for occupancy of 1–6 deuterium atoms for a vacancy in transition metals [53]. In EMT, the binding energy is defined as the energy required to embed a hydrogen atom into the host metal, and the hydrogen trapping energy in multiple occupancy is defined for the last hydrogen atom in VH_N complex as

$$\Delta E(N) = E(N) - E(N-1) - E^{\mathrm{sol}}, \tag{3.17}$$

where E^{sol} denotes the interstitial binding energy [53]. The observed profiles in Fig. 3.6 were in agreement with the ones calculated using trapping enthalpies of 61 kJ/mol for $N = 1$–2 and 41 kJ/mol for $N = 3$–6 [52]. The results implied decreasing trapping strength with increasing occupancy. Trapping energies calculated afterward using a modified EMT are included in Fig. 3.7 [54] with open circles.

Trapping energies for multiple hydrogen occupancy for a mono-vacancy were also calculated for iron using the density functional theory (DFT) [54, 55]. Calculated trapping energies of VH_N complexes in iron are shown in Fig. 3.7 together with the previous results of EMT calculations [53]. The DFT calculation shows that trapping energies of VH_1 and VH_2 are about 60 kJ/mol and that VH_6 is unstable. The calculation also shows that up to three hydrogen atoms are exothermically bound to mono-vacancy. Thus, very high site-occupancies of hydrogen are

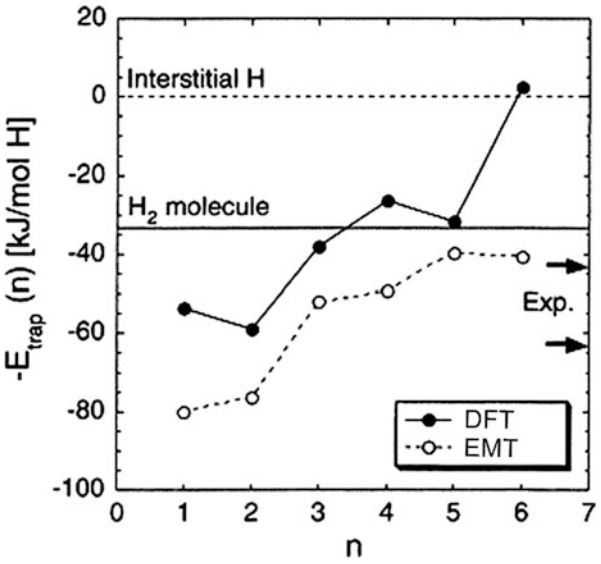

Fig. 3.7 Hydrogen trapping energy in α-Fe calculated using DFT (*filled circle*) and EMT (*open circle*) (Tateyama et al. [54], Reprinted with permission from American Physical Society)

expected for VH and VH_2 and most vacancies may exist in the form of VH_2 [55]. Another atomistic calculation using DFT combined with molecular dynamics and Monte Carlo methods [56] showed that a three-dimensional tetrahedral configuration has the lowest energy for VH_4 and the binding was exothermic.

An explanation of the stability deduced by the DFT analysis was that Fe3*d*-H1*s* hybridization causes charge transfer to the region around the hydrogen atom from neighboring iron atoms. Resulting negatively charged hydrogen atoms might repel each other, and distances between hydrogen atoms and the corresponding *O*-sites in the VH_N complexes were calculated to decrease with the increasing number of trapped hydrogen atoms *N* [54].

(b) Enhanced generation of vacancies

The increase in the hydrogen absorption capacity by plastic straining was revealed by means of hydrogen thermal desorption analysis (TDA) as shown in Fig. 3.2 for low-carbon ferritic steel. TDA profiles corresponding to the increase are shown in Fig. 2.4 for cold-drawn eutectoid steel. The increase in the hydrogen absorption capacity associated with plastic straining is enhanced when hydrogen is present at the time of straining. Figure 3.8 [57] shows the amount of hydrogen introduced to specimens of pure iron and Inconel 625 alloy as the tracer of defects. In Fig. 3.8, the tracer-hydrogen introduced to saturation into specimens is denoted as [strain], [H + strain] and [H + strain + 200 °C], each respectively indicating specimens "strained," "strained after hydrogen precharging" and "annealed at 200 °C after hydrogen precharging and straining." The enhanced increase by hydrogen precharging is generally observed for various steels and is in accord with the notion that hydrogen enhances the formation of strain-induced vacancies and their clustering, i.e., hydrogen-enhanced creation of strain-induced vacancies (HESIV).

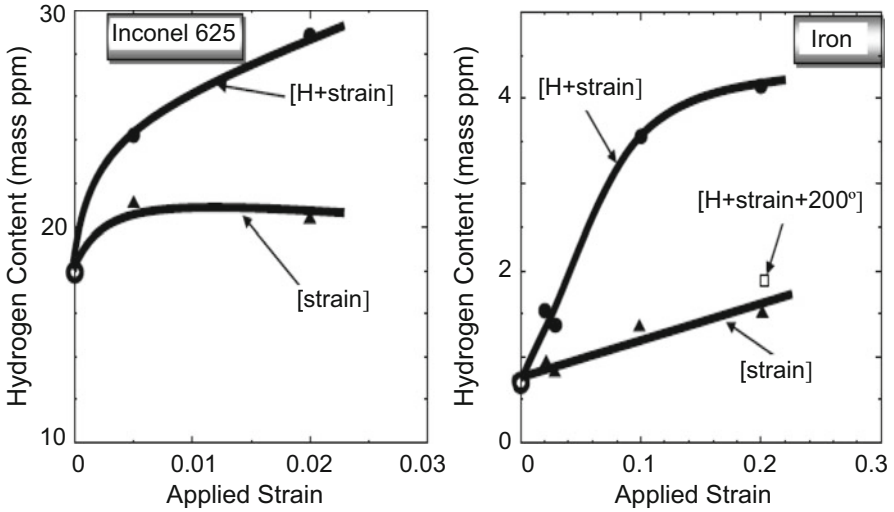

Fig. 3.8 The amounts of the tracer-hydrogen introduced to iron and Inconel 625 specimens after straining [strain], strained after hydrogen-precharging [H + strain] and further annealing at 200 °C [H + strain + 200 °C] (Takai et al. [57])

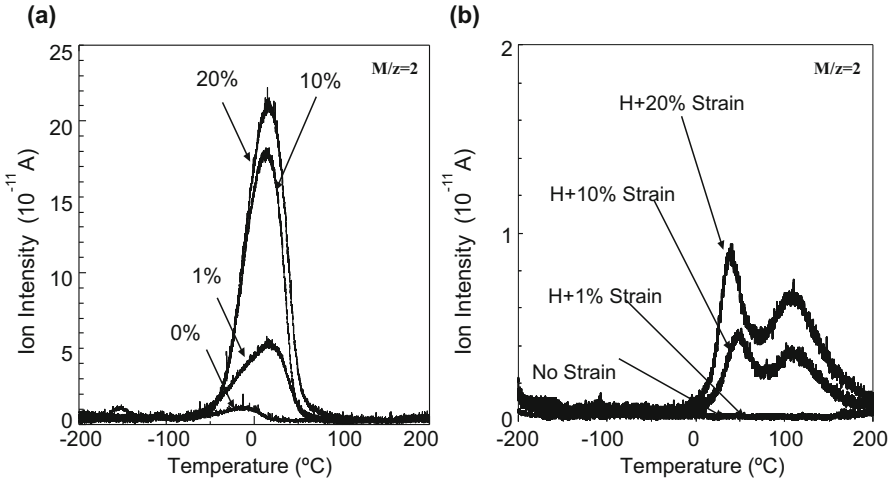

Fig. 3.9 LTDS profiles of hydrogen introduced into iron specimens given strain up to 40 % (**a**) without and (**b**) with hydrogen precharging. The thickness of specimen and the concentration of NH_4SCN are 0.3 mm and 20 % at 50 °C for (**a**) and 0.4 mm and 0.05 % at 30 °C for (**b**), respectively (Sato et al. [58], Abe et al. [59], Reprinted with permission from The Iron & Steel Inst. Japan)

The nature of strain-induced defects that interact with hydrogen has been examined by means of TDA and PAS. The low temperature thermal desorption spectroscopy (LTDS) described in Sect. 2.1.2(d) could firstly separate different strain-induced traps of diffusive hydrogen. Figure 3.9 [58, 59] shows LTDS profiles

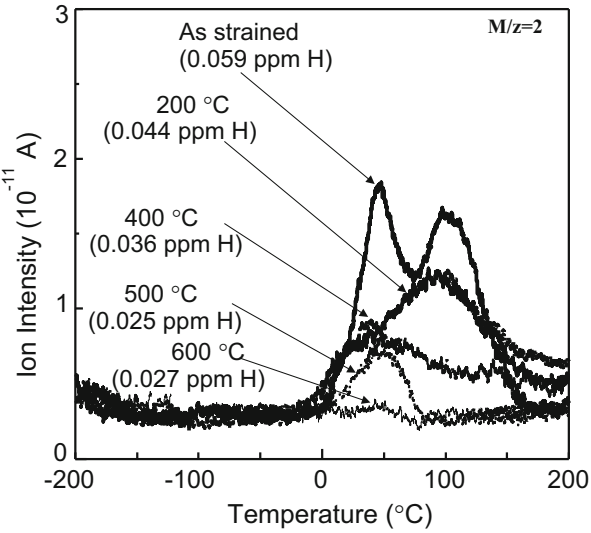

Fig. 3.10 LTDS profiles of hydrogen introduced into iron specimens given straining of 20 % and subsequent annealing at different temperatures. Hydrogen charging is by immersing specimens of 0.4 mm in thickness in a 0.05 mass % NH_4SCN aq at 30 °C for 6 h. Hydrogen contents are shown in brackets (Takai [60], By courtesy of Prof. K. Takai before publication)

of hydrogen introduced as the tracer of defects into specimens of pure iron given tensile strain up to 40 % with and without hydrogen precharging. Tracer-hydrogen was introduced by immersing specimens in aqueous solution of NH_4SCN. The amount of the tracer-hydrogen increases with strain, and effects of hydrogen precharging are characterized by a subpeak that appears at the higher-temperature side.

The strained specimens were then subjected to annealing at various temperatures, and hydrogen was again introduced as the tracer of defects.

Figure 3.10 [60] shows the change of LTDS profiles of the tracer-hydrogen with elevated annealing temperatures. The desorption at around 100 °C was substantially reduced by annealing at temperatures higher than 400 °C, while the lower temperature peak centered around 50 °C showed a two-step decrease firstly by annealing at 200 °C and completely at about 600 °C. The peak around 100 °C corresponds to the annihilation of vacancy clusters. The origin of the 50 °C peak is not definite. The changes in TDA profiles caused by annealing are due to not only the binding energy with traps but also to changes in the structure of trapping defects. As described in Sect. 3.2.3(a), deuterium implantation experiments revealed detrapping of deuterium from small vacancy clusters at 350–450 K. A possible origin of the substantial reduction of the low temperature peak by 200 °C annealing is reconfiguration of vacancy clusters associated with annealing and the resulted decrease in the affinity with tracer-hydrogen. A small further decrease in the 50 °C peak by annealing at 600 °C may be ascribed to the annihilation of dislocations trapping in which has been unable to detect by conventional TDA technique.

Positron annihilation spectroscopy (PAS) is a more direct method to reveal the nature of lattice defects as described in Sects. 3.2.1 and 3.2.2. Figure 3.11 [61] shows mean positron lifetimes τ_m in pure iron on isochronal annealing after tensile

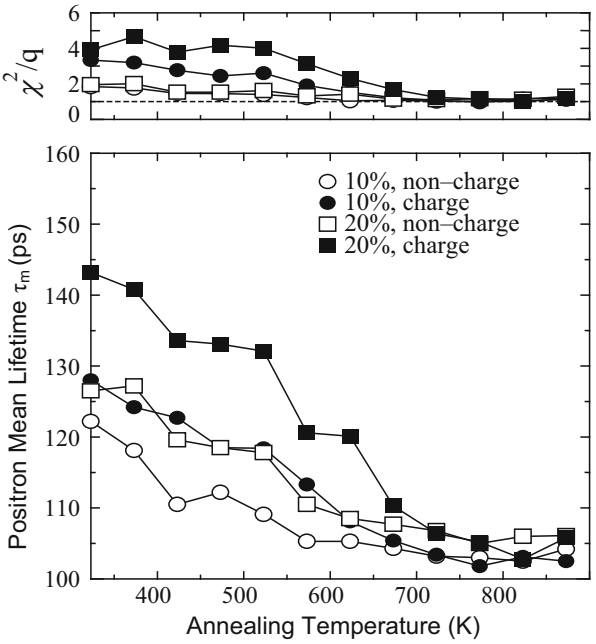

Fig. 3.11 Positron mean lifetime during isochronal annealing of iron deformed with and without hydrogen precharging. Filled marks denote hydrogen-precharged specimens (Sakaki et al. [61])

straining at room temperature with and without hydrogen precharging. The increase in τ_m by straining is enhanced by the presence of hydrogen at the time of straining. Annealing at 900 K reduced τ_m to 100 ± 2 ps which is coincident to the calculated τ in the α-Fe lattice [42]. The variances, χ^2/q, larger than 2.0 for τ_m in deformed iron indicate that τ_m is composed of multicomponents.

Significant recoveries of τ_m that appear at about 400 K, 550 K and 650 K were analyzed to components. Figure 3.12 [61] shows results for specimens deformed by 20 % (a) without and (b) with hydrogen precharging. In the annealing temperature range from 400 K to 625 K, the longer lifetime in two-component analyses was 150 ps that is coincident with a calculated τ in dislocations [62]. At temperatures lower than 375 K for (a) and 575 K for (b), three-component analyses gave the longest components τ_3 over 400 ps. The recovery stage corresponds to the annihilation of vacancies and τ_3 indicates positron lifetime likely in large vacancy clusters.

Figures 3.11 and 3.12 exhibit hydrogen effects that increase τ_m and retain the longest lifetime component τ_3 at high temperatures. The relative intensity of the τ_i component is related to the positron-trapping probability κ_i in Eq. (3.14) and κ_i is proportional to the concentration of the i-th defect C_i [35, 62]. The estimated densities of dislocations and vacancies are listed in Table 3.4 [61]. The density of dislocations increases with the amount of plastic strain as expected, but no effects of hydrogen appeared on the increase. On the other hand, a substantial enhancement by hydrogen is evident for the strain-induced generation of vacancies. This HESIV is consistent with the TDA results shown in Figs. 3.8 and 3.9 and manifests the preferential effect of hydrogen on strain-induced generation of vacancies rather than dislocations.

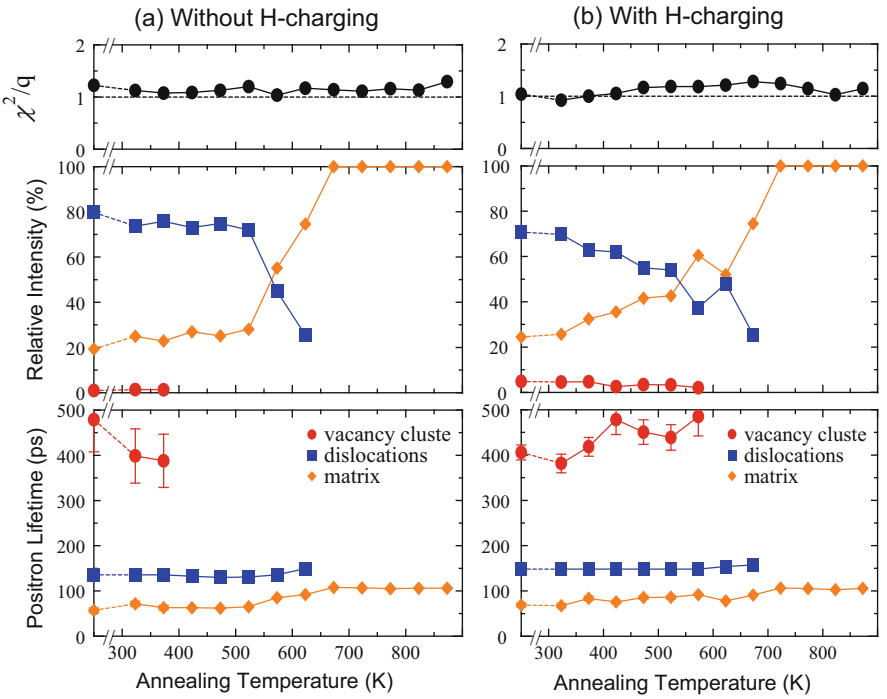

Fig. 3.12 Components of mean positron lifetimes shown in Fig. 3.11 and their relative intensities (Sakaki et al. [61])

Table 3.4 Densities of dislocations (C_d) and vacancies (C_V) in iron deformed with/without hydrogen precharging. Measurements by positron annihilation spectroscopy

Strain (%)	Hydrogen	C_d (10^{10}/cm^2)	C_V (10^{-7})
10	None	1	Not-detected
	Charged	0.9	1.7
20	None	2.2	1.7
	Charged	1.9	8.2

Sakaki et al. [60]

The thermal equilibrium density of vacancies increases with the decrease in the formation enthalpy of vacancies as Eq. (3.13) states. When the DEFACTANT mechanism by Kirchheim described in Sect. 3.1.2 is applied to vacancies with which hydrogen combines, the formation enthalpy of vacancies H_f is related to the logarithm of hydrogen activity as expressed in the form

$$\frac{\partial H_f}{\partial \ln a} = -\mathrm{RTZ}\,, \tag{3.18}$$

where Z is the average number of hydrogen atoms per vacancy [30]. A DFT calculation of the total energy of vacancy-hydrogen complex by Tateyama and

Ohno [54] showed a substantial decrease in H_f of VH_N, occasionally to negative values, under high hydrogen pressures of 1 ~ 2 GPa and Z of 5 or 6. However, expected densities of vacancies are still very low in thermal equilibrium in most situations where hydrogen embrittlement appears.

Another mechanism of realizing high densities of vacancies is kinetic effects. Excess vacancies generated by mutual interactions of dislocations are unstable and tend to annihilate at various sinks such as dislocations, grain boundaries and surfaces. Migration of vacancies is requisite for this process, but the formation of immobile clusters and of complexes with impurity atoms impede the migration as described in Sect. 3.2.2. Such states of vacancies retard annihilation and help to keep high densities before reaching thermal equilibrium.

The mobility of single vacancy in bcc iron under a hydrogen environment has been calculated using the DFT and the nudged elastic band method to find the diffusion path of the minimum energy [55]. A configuration, two hydrogen atoms trapped at opposite *O*-sites across a vacancy, has the highest binding energy, and the fraction of VH_2 complex is predominant at room temperature. In that configuration, the activation energy of diffusion of vacancy increases from 60 to 103 kJ/mol, and the frequency decreases from 1.71×10^{-2} to 1.62×10^{-8} s^{-1}, showing that the vacancy is almost immobile. As a consequence, in the case of vacancy generation by jog dragging of screw dislocations, high densities of vacancies are expected to remain behind moving screw dislocations [55].

3.3 Precipitates

Fine carbides or nitrides are widely utilized for grain refinement and precipitation hardening of steels. Interactions of hydrogen with such precipitates are important for hydrogen embrittlement of high strength steels, and many studies have been reported. Experiments to obtain binding energies mostly address diffusion or permeation processes in which hydrogen trapping and detrapping take place, as described in Sects. 2.1.2(b) and 3.1.1(b).

TiC is the most extensively studied precipitate. Asaoka et al. visualized the distribution of tritium introduced into a Fe-0.15%Ti alloy by means of tritium autoradiography and examined the thermal desorption and associated changes of the distribution of tritium [63]. Release of tritium from incoherent TiC/matrix interface took place at 600 °C, and the trapping enthalpy calculated using Oriani's diffusion equation [12] was 71–79 kJ/mol. The calculation, however, neglected the entropy term, and higher enthalpy values ~130 kJ/mol was estimated when the entropy term was taken into account.

Hydrogen thermal desorption analysis was applied by Lee and Lee to Fe-Ti-C alloys in which the amounts of Ti and C were varied in a wide range while fixing the Ti/C mass ratio at 4:1 [64]. Hydrogen was charged at 673 K under 0.1 MPa hydrogen gas, and the diffusive part of hydrogen was successively released at room temperature. TDA of remained hydrogen showed three desorption peaks at

473, 773 and 996 K at a heating rate of 3 K/min, and the 996 K peak was assigned to detrapping from the incoherent TiC/matrix. The activation energy of detrapping obtained from Kissinger's equation, Eq. (2.7), was 86.9 kJ/mol. The binding energy of hydrogen with TiC was calculated using the relation between the TDA peak area and the hydrogen-charging temperature T_{H} of the form

$$C_x = N_x C_0 \exp\left(\frac{E_b - E_0}{RT_H}\right), \tag{3.19}$$

where C_x and C_0 are respectively concentrations of hydrogen trapped at TiC and in solid solution, N_{x} is the trap density and E_0 is the heat of solution [64]. The estimated binding energy $E_{\mathrm{b}}^{\mathrm{TiC}}$ and N_{x} are 28.1 kJ/mol and 10^{23}/cm^3-Fe, respectively.

Alternatively, TDA was conducted for specimens with controlled TiC/matrix interfaces [65]. Hydrogen introduced to a ferritic Fe-Ti-C alloy heat-treated at different austenitizing temperatures showed four desorption peaks at 383, 473, 748 and 880 K at a heating rate of 3 K/min. Two peaks at 748 K and 800 K were assigned to detrapping from semi-coherent and incoherent interfaces, respectively. It implies that the trapping strength of TiC increases associated with the loss of particle/interface coherency. It is to be noticed that the hydrogen trapping energy at the incoherent interface is not always unique. The peak temperature assigned to incoherent interface shifted to higher temperatures when specimens were further heat-treated to increase the TiC particle size.

In ferritic Fe-Ti-C alloys, incoherent TiC particles and Ti atoms in solution act as irreversible and reversible traps, respectively. The apparent diffusion coefficient obtained by permeation transient is often used to estimate the binding energy of hydrogen with traps as described in Sect. 3.1.1(b). A sequential permeation method was devised to separate trapping parameters of reversible and irreversible traps [66]. Both types of trapping take place in the first permeation, but reversible trapping dominates diffusivity in the second transient after irreversible traps have been filled. Irreversible trapping parameters were obtained from the difference between the first and the second transients. The obtained binding energies were 94.6 kJ/mol for incoherent TiC and 26 kJ/mol for reversible trap assigned to solute Ti atom [66]. Precipitation of TiC on tempering of martensitic steels brings about a substantial increase in hydrogen absorption capacity, but the distinction between coherent and incoherent precipitation for the increase is not definite [67].

NbC and VC that take NaCl-type structures are also common precipitates in high strength low alloy steels, and their precipitation increases hydrogen absorption capacities of steels. Desorption peak temperatures on TDA relevant to NbC and VC are generally lower than the peak temperature due to TiC [68, 69] but are often in the same range as desorption from other traps. Determination of specific trapping parameters is difficult, but lower peak temperatures imply lower binding energies of hydrogen with NbC and VC than that with TiC. Figure 3.13 [70] shows TDA profiles of hydrogen introduced to 0.37C-1.0Mo-0.54 V martensitic steel tempered at different temperatures. The precipitation of fine VC particles causes a prominent

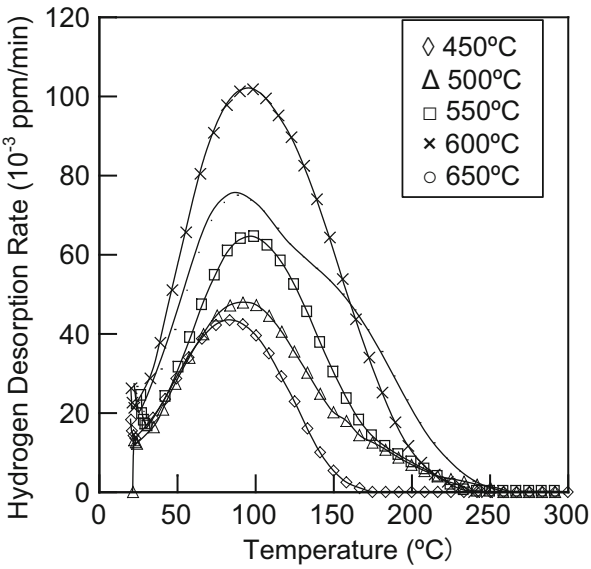

Fig. 3.13 TDA profiles of hydrogen introduced to 0.37C-1.0Mo-0.54 V martensitic steel tempered at temperatures shown in the insert (Nagumo et al. [70])

secondary hardening of martensite. Separately conducted hardness measurements and transmission electron microscopy revealed that the increase in the hydrogen absorption capacity was associated with secondary hardening [69]. A distinct shoulder in the high-temperature side of the desorption peak for 650 °C tempering is ascribed to trapping at fine VC precipitates.

An important subject on interactions of hydrogen with precipitates is effects of applied stress or plastic strain. In previous sections, the hydrogen-enhanced creation of strain-induced vacancies is presented, where vacancies act as traps of diffusive hydrogen. Interactions of hydrogen with fine VC precipitates were examined under applied stress for Mo-V steel [70]. Figure 3.14 [70] shows TDA profiles of hydrogen introduced to specimens under simultaneous loading. The specimens were tempered at 550 °C and 650 °C, and the applied stress was 0.4 of the ultimate tensile strength. In Fig. 3.14, the filled marks indicate TDA profiles after degassing at room temperature for 24 h. The difference between the open and filled marks is the amount of diffusive hydrogen. TDA curves exhibit a single peak, but the peak widths are fairly wide. Room temperature degassing showed that hydrogen composing the higher-temperature side of the peak is nondiffusive. A separately conducted measurement showed that the applied stress increased densities of trap sites of both diffusive and nondiffusive hydrogen [70], and that the increase was more prominent for nondiffusive one.

The results indicate that applied stress enhances strong hydrogen trapping by VC. The number of precipitates, i.e., of the hydrogen trapping sites, is much higher and their distribution is more uniform by tempering at 650 °C than at 550 °C. On the other hand, weakly trapped diffusive hydrogen is crucial to degradation. It should be noticed that the overall or average information from a specimen does not always

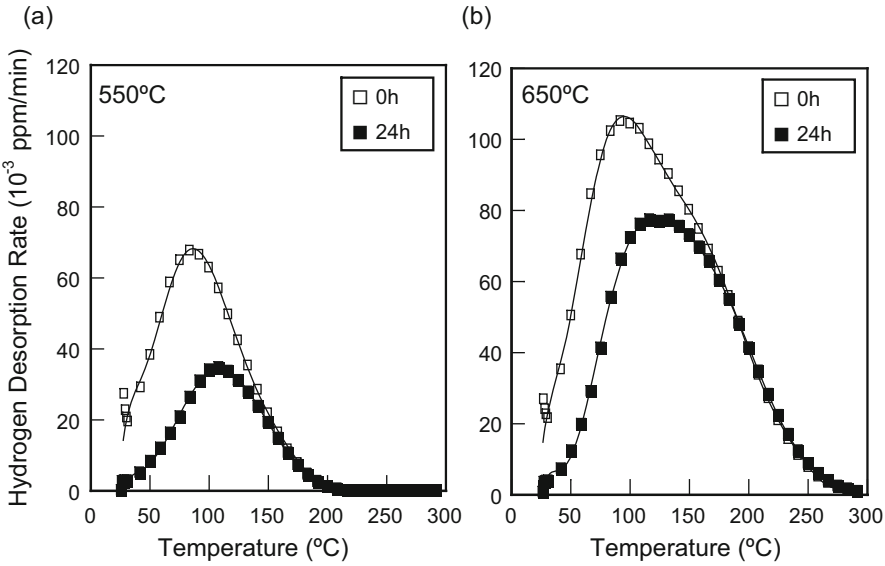

Fig. 3.14 TDA profiles of hydrogen introduced to 0.37C-1.0Mo-0.54 V martensitic steel tempered at (**a**) 550 °C and (**b**) 650 °C. Hydrogen charging is conducted under applied stress of 0.4 tensile strength. Filled marks denote specimens kept for 24 h at 30 °C to remove diffusive hydrogen (Nagumo et al. [70])

represent local situations crucial to fracture events. Details of hydrogen trapping behaviors concerning hydrogen embrittlement are described in Sect. 8.1(b).

Precipitation of fine Fe_3C hardly affects the hydrogen absorption capacity on tempering of 0.42 % C martensitic steel [67]. TDA profiles of hydrogen in eutectoid steel does not show trapping of hydrogen to pearlitic Fe_3C when cold-working is not applied as shown in Fig. 2.4. It suggests that Fe_3C and its interface are not strong trap sites. On the other hand, two TDA peaks appeared by cold-drawing originated in fine lamellar Fe_3C. The appearance of higher-temperature peak and its increase by cold-drawing are surely due to the strain-induced formation of irreversible traps in the interface or within Fe_3C. A noteworthy fact is that such irreversibly trapped hydrogen or trapping defects are almost immune to hydrogen embrittlement.

3.4 Grain Boundaries

Accumulation of hydrogen along grain boundaries has been revealed directly by means of tritium autoradiography as shown in Fig. 2.12 for ferritic steel. However, types and structures of grain boundaries are diverse, and quite different values have been reported for binding energies of hydrogen with grain boundaries. Thermal desorption kinetics and tritium autoradiography for ferritic Fe-Ti-C alloys showed that the release of tritium from grain boundaries took place below 300 °C and the

calculated trapping energy was 59 kJ/mol, neglecting the entropy term in the free energy change [63].

The binding energy of hydrogen with ferrite grain boundaries in iron was also reported from TDA measurements [14]. The grain size of cold-worked iron was widely controlled from two to nine in the ASTM numbers by recrystallization. A TDA peak that appeared around 373 K preceding the evolution of a large desorption peak was assigned to grain boundaries. The activation energy of desorption obtained using Kissinger's equation was 17.2 kJ/mol, giving 9.6 kJ/mol for the binding energy after subtracting the saddle point energy of 7.6 kJ/mol. However, Kissinger's equation implicitly addresses the dissociation-controlled desorption of hydrogen, and the value of 9.6 kJ/mol is too small to apply the analysis. For the experiment, the specimen was 8 mm in diameter and degassing at room temperature for 6 h was given, but excess solute hydrogen might have remained. Alternatively, modeling of TDA profiles of hydrogen from pure iron with different grain size was conducted assuming diffusion-controlled desorption [15] as described in Sect. 2.1.2 (b). The desorption-rate peak at 415 K was assigned to grain boundaries, and the binding energy of 49 kJ/mol gave the best fit between simulated and experimental TDA profiles.

Prior austenite grain boundaries in martensitic steels are often decorated with impurity segregation and precipitates. However, observed accumulation of hydrogen along grain boundaries does not necessarily induce intergranular fracture. The role of grain boundaries in hydrogen embrittlement is to be considered taking into account various factors, not only cohesive strength of boundaries and its modifications by segregated impurities or precipitates but also concentrated plastic deformation in adjacent areas.

3.5 Voids and Surfaces

Formation of small voids or cracks is feasible in deformed metallic materials, and such defects are activated by the precipitation of molecular hydrogen under high hydrogen fugacity. Detrapping of deuterium from helium bubbles formed by ion implantation of 15-keV ^{4}He into iron and austenitic stainless steels was investigated by measuring the release of deuterium [46, 47]. The size of bubbles was about 1 nm in diameter, and the thermal release of deuterium from the implanted zone was analyzed in the same way as described in Sect. 3.2.3(a). For iron, three types of traps were assumed, and the strongest trap with the binding enthalpy of 75 kJ/mol was assigned to detrapping from He bubbles [46]. Similarly in a Type 304 stainless steel, the corresponding value was 41 kJ/mol assuming two types of traps [47].

When molecular hydrogen in voids diffuses out, adsorption on the void surface is requisite as an intermediate step, and the binding of deuterium with He bubble is considered as chemisorption-like interaction. The binding energy of hydrogen with the bubble surface E_T is the lowering of the hydrogen energy relative to lattice site as illustrated in Fig. 3.15 [71]. It is written as

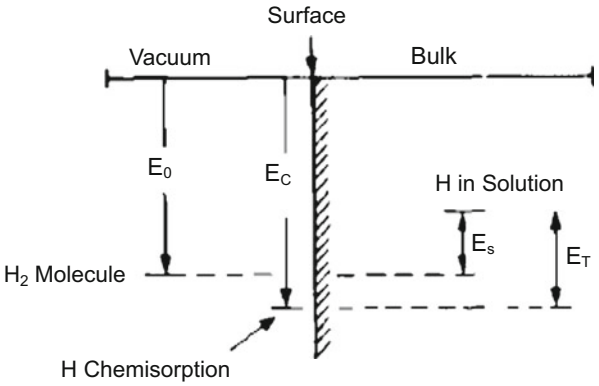

Fig. 3.15 Schematic illustration of hydrogen energies. E_T is the lowering of hydrogen energy by moving from solutionized bulk to surface site (Picraux [71])

$$E_T = E_{\text{chem}} + E_s - \frac{1}{2}E_{H_2}\,, \tag{3.20}$$

where E_{chem} is the chemisorption binding energy of hydrogen referred to the free hydrogen atom in vacuum, E_s is the heat of solution and E_{H2} is the energy of hydrogen molecule. Using experimental values of $E_{\text{chem}} = 259$ kJ/mol and $E_s = 28$ kJ/mol together with $E_0 = 222$ kJ/mol for α-Fe, a calculated E_T is 77 kJ/mol [71]. The calculated value of E_T is consistent with the value obtained from the deuterium implantation experiment [46].

References

1. R. Gibara, A.J. Kumnick, in *Hydrogen Embrittlement and Stress Corrosion Cracking*, ed. by R. Gibara, R.F. Hehemann (ASM, Metals Park, 1984), pp. 61–77
2. T.S. Kê, Scr. Metall. **16**, 225–231 (1982)
3. V. Hivert, P. Groh, W. Frank, I. Ritchie, P. Moser, Phys. Status Solidi (a), **46**, 89–98 (1978)
4. G.M. Sturges, A.P. Miodownik, Acta Metall. **17**, 1197–1207 (1969)
5. J.P. Hirth, Metall. Trans. A **11A**, 861–890 (1980)
6. G. Schoek, Scr. Metall. **16**, 233–239 (1982)
7. A. Seeger, Scr. Metall. **16**, 241–247 (1982)
8. J.P. Hirth, Scr. Metall. **16**, 221–223 (1982)
9. A. Zielinski, E. Lunarska, M. Smialowski, Acta Metall. **25**, 551–556 (1977)
10. R. Gibara, Trans. Metall. Soc. AIME **239**, 1574–1585 (1967)
11. S. Asano, M. Shibata, Scr. Metall. **16**, 1171–1174 (1982)
12. R.A. Oriani, Acta Metall. **18**, 147–157 (1970)
13. A.J. Kumnick, H.H. Johnson, Acta Metall. **28**, 33–39 (1980)
14. W.Y. Choo, J.Y. Lee, Metall. Trans. A **13A**, 135–140 (1982)
15. K. Ono, M. Meshii, Acta Metall. **40**, 1357–1364 (1992)
16. M. Nagumo, K. Ohta, H. Saitoh, Scr. Mater. **40**, 313–319 (1999)
17. J.P. Hirth, in *Hydrogen Degradation of Ferrous Alloys*, ed. by R.A. Oriani, J.P. Hirth, M. Smialowski (Noyes Pub., Park Ridge, 1985), pp. 131–139
18. J.P. Hirth, B. Carnahan, Acta Metall. **26**, 1795–1803 (1978)
19. S. Taketomi, R. Matsumoto, N. Miyazaki, Acta Mater. **56**, 3761–3769 (2008)

20. J.W. Christian, Metall. Trans. A **14A**, 1237–1256 (1983)
21. M.S. Duesbery, V. Vitek, Acta Mater. **46**, 1481–1492 (1998)
22. M. Wen, A.H.W. Ngan, Acta Mater. **48**, 4255–4265 (2000)
23. S.L. Frederiksen, K.W. Jacobsen, Philos. Mag. **83**, 365–375 (2003)
24. M. Itakura, H. Kaburaki, M. Yamaguchi, Acta Mater. **60**, 3698–3710 (2012)
25. M. Wen, S. Fukuyama, K. Yokogawa, Acta Mater. **51**, 1767–1773 (2003)
26. M. Itakura, H. Kaburaki, M. Yamaguchi, T. Okita, Acta Mater. **61**, 6857–6867 (2013)
27. V.G. Gavriljuk, V.N. Shivanyuk, B.D. Shanina, Acta Mater. **53**, 5017–5034 (2005)
28. V.G. Gavriljuk, B.D. Shanina, V.N. Shivanyuk, S.M. Teus, J. Appl. Phys. **108**, 083723 (2010)
29. R. Kirchheim, Acta Mater. **55**, 5129–5138 (2007)
30. R. Kirchheim, Acta Mater. **55**, 5139–5148 (2007)
31. R. Kirchheim, Scr. Mater. **62**, 67–70 (2010)
32. H.J. Wollenberger, in *Physical Metallurgy*, ed. by R.W. Cahn, P. Hansen, vol. II, 4th edn. (North-Holland, Amsterdam, 1996), Chapter 18
33. R.W. Siegel, J. Nucl. Mater. **69&79**, 117–146 (1978)
34. P. Hautojä, in *Characterization of Defects in Materials*, ed.. by R.W. Siegel, J.R. Weertman, R. Sinclair, Materials Research Society Proceedings, vol. 82 (MRS, 1987), pp. 3–21
35. A. Vehanen, P. Hautojärvi, J. Johansson, J. Yl-Kauppila, P. Moster, Phys. Rev. B **25**, 762–780 (1982)
36. L. De Schepper, D. Segers, L. Dorikens-Vanpraet, M. Dorikens, G. Knuyt, L.M. Stals, P. Moser, Phys. Rev. B **27**, 5257–5269 (1983)
37. J. Takamura, I. Takahashi, M. Amano, Trans. ISIJ **9**, 216–221 (1969)
38. H.G. van Bueren, Acta Metall. **3**, 519–524 (1955)
39. A.M. Cuttiño, M. Ortiz, Acta Mater. **44**, 427–436 (1996)
40. U. Essmann, H. Mughrabi, Philos. Mag. A **40**, 731–756 (1979)
41. J.R. Beeler Jr., R.A. Johnson, Phys. Rev. **156**, 677–684 (1967)
42. M.J. Puska, R.M. Nieminen, J. Phys. F: Met. Phys. **13**, 333–346 (1983)
43. M. Kiritani, H. Takata, K. Moriyama, F.E. Fujita, Philos. Mag. A **40**, 779–802 (1979)
44. R.W. Balluffi, J. Nucl. Mater. **69&70**, 240–263 (1978) (Overview)
45. S.M. Myers, S.T. Picraux, R.E. Stolts, J. Appl. Phys. **50**, 5710–5719 (1979)
46. S.M. Myers, D.M. Follstaedt, F. Besenbacher, J. Bøttiger, J. Appl. Phys. **53**, 8734–8744 (1982)
47. S.M. Myers, W.R. Wampler, F. Besenbacher, J. Appl. Phys. **56**, 1561–1571 (1984)
48. F. Besenbacher, J. Bøttiger, S.M. Myers, J. Appl. Phys. **53**, 3536–3546 (1982)
49. F. Besenbacher, B.B. Nielson, S.M. Myers, J. Appl. Phys. **56**, 3384–3393 (1984)
50. S.M. Myers, F. Besenbacher, J. Appl. Phys. **60**, 3499–3507 (1986)
51. F. Besenbacher, J. Bøttiger, B.B. Nielson, A.A. Pisarew, Phys. Rev. Lett. **49**, 1420–1422 (1982)
52. F. Besenbacher, S.M. Myers, P. Nordlander, J.K. Nørskov, J. Appl. Phys. **61**, 1788–1794 (1987)
53. P. Nordlander, J.K. Nørskov, F. Besenbacher, S.M. Myers, Phys. Rev. B **40**, 1990–1992 (1989)
54. Y. Tateyama, T. Ohno, Phys. Rev. B **67**, 174105 (2003)
55. R. Matsumoto, N. Nishiguchi, S. Taketomi, N. Miyazaki, J. Soc. Mater. Sci. Jpn. **63**, 182–187 (2014)
56. E. Hayward, B. Beeler, C. Deo, Philos. Mag. Lett. **82**, 217–225 (2012)
57. K. Takai, H. Shoda, H. Suzuki, M. Nagumo, Acta Mater. **56**, 5158–5167 (2008)
58. Y. Sato, T. Doshida, H. Suzuki, K. Takai, Y. Hagiwara, CAMP-ISIJ **23**, 1292 (2010)
59. N. Abe, H. Suzuki, K. Takai, N. Ishikawa, H. Sueyoshi, in *Environmentally Assisted Cracking of Materials*, Proceedings MS&T 2011 (2011), pp. 1277–1284
60. By courtesy of Prof. K. Takai for results before publication
61. K. Sakaki, T. Kawase, M. Hirano, M. Mizuno, H. Araki, Y. Shirai, M. Nagumo, Scr. Mater. **55**, 1031–1034 (2006)
62. C. Hidalgo, G. González-Doncel, S. Linderoth, J. San Juan, Phys. Rev. B **45**, 7017–7021 (1992)

63. T. Asaoka, C. Dagbert, M. Autocouturier, J. Galland, Scr. Metall. **11**, 467–472 (1977)
64. H.G. Lee, J.Y. Lee, Acta Metall. **32**, 131–136 (1984)
65. S.M. Lee, J.Y. Lee, Acta Metall. **35**, 2695–2700 (1987)
66. G.M. Pressouyre, I.M. Bernstein, Metall. Trans. A **9A**, 1571–1580 (1978)
67. F.-G. Wei, T. Hara, T. Tsuchida, K. Tsuzaki, ISIJ Int. **43**, 539–547 (2003)
68. T. Omura, T. Kushida, K. Miyata, Y. Komizo, Tetsu-to-Hagané **90**, 106–112 (2004)
69. T. Tsuchida, T. Hara, K. Tsuzaki, Tetsu-to-Hagané **88**, 771–778 (2002)
70. M. Nagumo, T. Tamaoki, T. Sugawara, in *Hydrogen Effects on Materials Behavior and Corrosion Deformation Interactions*, ed. by N.R. Moody, A.W. Thompson, R.E. Ricker, G.W. Was, R.E. Jones (TMS, Warrendale, 2003), pp. 999–1008
71. S.T. Picraux, Nucl. Inst. Methods **182/183**, 413–437 (1981)